Modelling bioactivity and degradation of bioactive glass based tissue engineering scaffolds

J.A. Sanz-Herrera [a,b,*], A.R. Boccaccini [c,d]

[a] School of Engineering, University of Seville, 41092 Seville, Spain
[b] CIBER-BBN Centro Investigación Biomédica en Red en Bioingeniería, Biomateriales y Nanomedicina, 50018 Zaragoza, Spain
[c] Department of Materials, Imperial College London, London SW7 2BP, UK
[d] Institute of Biomaterials, Department of Materials Science and Engineering, University of Erlangen-Nuremberg, 91058 Erlangen, Germany

ARTICLE INFO

ABSTRACT

Bioactive glasses are a class of inorganic biomaterials widely used in bone tissue engineering and regenerative medicine. Once implanted in the human body, these biomaterials react with the body fluid resulting in the formation of a surface hydroxyapatite (HA) layer, which exhibits the ability to form a stable chemical bond with the adjacent living bone tissue. The experimental evaluation of the degradation of bioactive glasses in contact with body fluid requires long-term in vitro assays. In this work, a novel mathematical model is proposed to numerically analyze the dissolution and bioactivity of bioactive glasses in relevant conditions for their in vitro and in vivo applications. A detailed framework is described for the numerical implementation using the Voxel-FEM method, in order to account for the microstructural evolution as consequence of degradation and HA layer formation. Two examples of application are highlighted, showing the suitability and usefulness of the proposed model for the evaluation of bioactive glasses in tissue engineering applications.

1. Introduction

Bioactive silicate glasses were discovered by Hench et al. (1971) almost 40 years ago. When implanted in the human body, these glasses react with the body fluid, which dissolves the glasses through complex surface physico-chemical reactions. Glass dissolution releases a cascade of ions, which in turn react with the body fluid finally resulting in the formation of a surface hydroxyapatite (HA) layer. Due to the presence of this layer, the biomaterial exhibits the ability to form stable chemical bonds with the adjacent living tissue (Hench et al., 1971; Hench, 1998). This particular behaviour is known as 'bioactivity' in the specialised literature (Kokubo et al., 1990). One of the most popular bioactive glasses has the composition 45 wt.% SiO_2, 24.5 wt.% Na_2O, 24.5 wt.% CaO and 6 wt.% P_2O_5, and it is known as 45S5 Bioglass® (Hench et al., 1971). This bioactive glass has been the base material for many developments in the framework of (non-load bearing) orthopaedic implants, dental materials as well as regenerative medicine and bone tissue engineering, showing promising results in several cases and applications (i.e., see Chen et al., 2006a; Hench and Paschall, 1973; Hench et al., 1991; Hench and West, 1996; Rezwan et al., 2006; Roether et al., 2002a,b; Wilson and Low, 1992; Wilson et al., 1993; Yamamuro, 1990).

The intrinsic behaviour of bioactive glasses has placed these materials as perfect candidates for fabrication of scaffolds for bone tissue engineering applications (Chen et al., 2006a; Hench and Polak, 2002; Rezwan et al., 2006; Roether et al., 2002a). In this field, highly porous scaffolds are used as substrates to promote new bone tissue formation. Among many requirements, the scaffold should be porous with adequate pore size, exhibit tailored degradation/dissolution and must be strong enough to support mechanical loads (mainly in bone tissue applications) (Guarino et al., 2007; Hutmacher, 2000; Jerome and Maquet, 1997; Wake et al., 1994). Fabrication techniques to produce suitable porous scaffolds from bioactive glasses (and glass–ceramics) have been reported (Chen et al., 2006a; Fu et al., 2007; Livingston et al., 2002; Vitale-Brovarone et al., 2007).

In terms of structural integrity, bioactive glasses are not optimal materials due to their intrinsic brittleness (Chen et al., 2006a). Some solutions in this context are either forming a crystalline phase in the bioactive bulk glass, effectively developing glass–ceramics (Chen et al., 2006a; Vitale-Brovarone et al., 2007), or introducing a different phase (usually a polymer), forming a composite (Yunos et al., 2008).

Scaffold performance evaluation is crucial to ensure a well-designed tissue engineering scaffold. Experimental protocols may

* Corresponding author at: School of Engineering, University of Seville, Camino de los descubrimientos s/n, 4 41092 Seville, Spain. Tel.: +34 954 486079; fax: +34 954 487295.
   E-mail address: jsanz@us.es (J.A. Sanz-Herrera).

be classified into in vivo and in vitro tests. In vivo tests carried out on scaffolds usually involve a multidisciplinary team including tasks like scaffold characterization, scaffold implantation, histologies, bone quantification or scaffold dissolution. On the other hand, in vitro characterization of scaffolds includes mechanical characterization in terms of toughness, stiffness, constitutive behaviour as well as biodegradation, among many other assays. Therefore, both in vivo and in vitro evaluation of scaffold behaviour require a great amount of facilities and long-term setups (e.g. a biodegradation assay usually takes 21 days for bioactive glasses). In this scenario, numerical prediction of scaffold behaviour represents a very useful alternative for scaffold design, once a proper validation is conducted.

For example, overall mechanical properties of scaffolds may be numerically obtained using the homogenization theory (Lin et al., 2004; Sanz-Herrera et al., 2008b). The suitability of this theory was experimentally corroborated recently for the evaluation of the mechanical properties and the permeability of scaffolds (Sanz-Herrera et al., 2008c). Moreover, the complex evolution of the mechanical behaviour of a scaffold as new bone tissue grows has been simulated (Sanz-Herrera et al., 2008d).

Very few works have been developed to numerically analyze degradation/dissolution of biomaterials. Adachi et al. (2006) developed a numerical approach to simulate degradation and erosion, by the implementation of a model previously introduced by Gopferich (1997) available for polymeric biomaterials. The phenomenon of erosion was simulated in this work using the Voxel Finite Element Method (Voxel-FEM) (Adachi et al., 2001; Guldberg et al., 1998). This model was also applied in a multiscale formulation of bone growth and scaffold resorption for polymeric scaffolds (Sanz-Herrera et al., 2009a).

Recently, Wang et al. (2009) and Han and Pan (2009) presented a novel model to analyze degradation of biopolymers. The model was established from a continuum approach based on reaction–diffusion equations. The phenomenon of erosion, however, was not explicitly modelled in their work. Other important issues in bioactive glasses, such as bioactivity, have been investigated and modelled by means of a molecular dynamics (MD) framework (see Tilocca, 2009 for a review). MD simulation allows the specific and rigorous study of some events that take place during dissolution and bioactivity phenomena at the atomic level. MD numerical approaches include the analysis of the atoms and ions involved in the related physico-chemical reactions in order to add some information regarding glasses nanostructure, atomic groups role on bioactivity or clustering (Tilocca, 2009). However, there exist a gap between information provided by MD models and its implication in the overall macroscopic behaviour. In contrast, a pure macroscopic approach itself requires phenoenological feedback. Both kind of models are then complementary and necessary to get insight on the behaviour of bioactive glasses.

In this paper, a novel theoretical model for the analysis and simulation of dissolution and bioactivity of bioactive glasses is presented. The model starts rationally from the study and analysis of the fundamental reaction equations of dissolution and precipitation that take place in bioactive glasses, finally yielding to reaction–diffusion equations. Model parameters implications and assumed boundary conditions are discussed in detail. The obtained set of differential equations allows to phenomenologically model dissolution and precipitation, as a measure of bioactivity. The phenomenon of biomaterial dissolution is numerically simulated through the Voxel-FEM method. Two examples of applications are shown: the first one regards a parametric analysis that highlights the influence of some of the most important model parameters, discussing their physical meaning in terms of their mathematical definition. The second example represents an actual Bioglass® based scaffold microarchitecture. The aim of this example is to show the potential and usefulness of the proposed theoretical model on an actual biodegradation in vitro test. Results are qualitatively validated, to some extent, with experimental results.

2. Model equations for bioactivity and dissolution

2.1. Problem description

The model is rationally based on the chemistry and underlying phenomena that take place once a bioactive glass specimen is immersed in a simulated body fluid (SBF) (Hench, 1998). In vitro tests in SBF are currently used to study bioactivity of materials, representing usually the first test carried out on biomaterials to detect the formation of HA, which should lead to strong bond to bone tissue (Hench, 1998; Kokubo et al., 1990). Before describing in detail the model equations, the main fundamental issues about the dissolution of bioactive glass derived tissue engineering scaffolds are addressed in this section.

For fabrication of scaffolds from melt-derived Bioglass® powder, a foam replica technique involving sintering at high temperature (>1000°) has been developed (Chen et al., 2006a). The heat-treatment results in partial crystallisation of the foam struts. It has been reported that an excessively crystalline degree may turn the glass into an inert material (Li et al., 1992). However, in highly porous scaffolds, crystallisation of the Bioglass® matrix induces only a retardation of the HA formation in contact with simulated body fluid due to the increased surface area in direct contact with the fluid (Chen et al., 2006a).

Once the biomaterial is implanted in vivo or immersed in vitro (e.g. in SBF) the bioreactivity of bioactive glasses leads to a cascade of reactions, which may be summarized through a sequence of five consecutive steps (Clark et al., 1976; Hench, 1998): (i) Na^+ ions are rapidly released at the surface and replaced by H^+ from the SBF solution, (ii) the corresponding increase in local pH promotes breaking of surface Si–O–Si bonds and release of soluble silica to the SBF solution, (iii) some of the surface silanol groups formed in steps (i) and (ii) condense to form a hydrated silica-rich layer on the surface, depleted in modifier cations, (iv) calcium and phosphate ions are released through the surface silica layer, and incorporate other Ca^{2+} and PO_4^{3-} from the SBF solution to form an amorphous calcium phosphate phase deposited on the surface, and (v) the latter amorphous film incorporates additional carbonate ions from solution and crystallizes to hydroxycarbonate apatite.

Similarly the partially crystallised Bioglass®-based scaffold exhibits surface reactions in contact with SBF, in particular the crystalline phase dissolves first (Chen et al., 2006a). The mechanism of dissolution in this case can be explained through three main phenomena (Boccaccini et al., 2007): (i) preferential dissolution at glass/crystal interfaces, (ii) break-down of crystalline particles into very fine grains through preferential dissolution at crystal structural defects, and (iii) amorphisation of the crystalline structure by introduction of point defects produced during ion exchange. From this step, the sequence of reactions mentioned above for Bioglass® are thought to take place and HA forms (Boccaccini et al., 2007; Chen et al., 2006a).

In the present study, both the process of bioactivity and dissolution are modelled in a simplified way. Four main species are considered in our model:

- *SBF* [mol/m³] which is a model aqueous solution in contact with the biomaterial.
- *Bioactive glass (BG)* [mol/m³] which represents the overall constituent of the scaffold and reacts with the SBF, as outlined above.
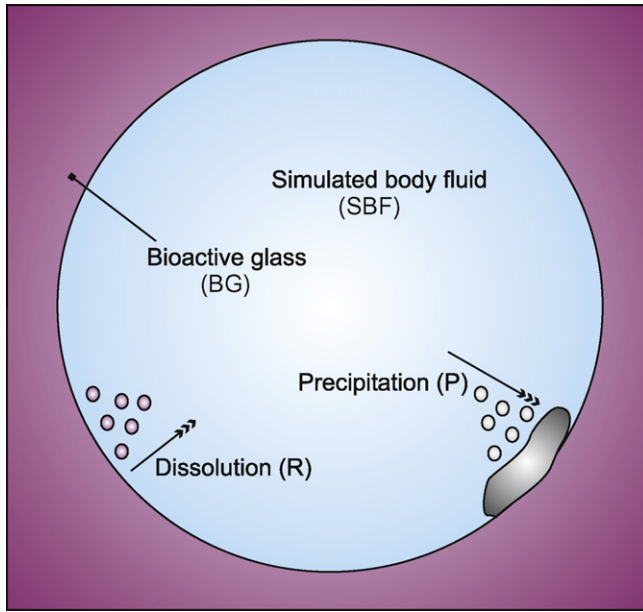
Fig. 1. Different species identified in the model and their implication in the dissolution–precipitation reactions.

- *Reactant aqueous solution (R)* [mol/m³] which represents the overall dissolved products (cations and anions) resulting from the reaction between the (partially crystallised) bioactive glass scaffold and the SBF.
- *Precipitate (P)* [mol/m³] which represents the overall nucleated products deposited on the biomaterial surface.

As a simplification, we do not explicitly consider the precipitation of both the silica and HA layers but they are globally featured by the precipitate layer (P). According to the considered species and the explained reactions that take place, we can write the following equation for the dissolution of the BG species:

$$n_{sd} \cdot SBF(aq) + n_b \cdot BG(s) \rightarrow n_{rd} \cdot R(aq) + \text{others}_d \qquad (1)$$
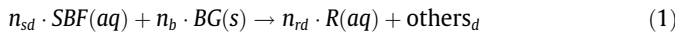
where n_{sd}, n_b and n_{rd} are the molar (stechiometric) proportions of the involved species in the dissolution reaction. others$_d$ represent some other species involved in the dissolution reaction. It is considered they have a minor relevance and were neglected as a first approach. We consider that the species SBF and R can diffuse into the bulk biomaterial. This is a consequence of the micropores and eventually microcracks formed during the fabrication of the scaffold (Chen et al., 2006a). Therefore, the dissolution equation (1) applies to the entire domain (not only to the surface). Eq. (1) macroscopically represents thus the phenomenon of crystal dissolution and break-down of crystalline particles explained above since the glass–crystal material is assumed as a homogeneous continuum (see Fig. 1). Moreover, the release of reactant constituents—featured by R—in the solution, enables the cascade of reactions mentioned above to occur in contact with SBF. These reactions first result in the formation of a silica layer on the scaffold surface to finally yield the HA layer, as explained above. This process is simplified by considering an overall unique[1] precipitation reaction according to the following expression:

$$n_{sp} \cdot SBF(aq) + n_{rp} \cdot R(aq) \rightarrow n_p \cdot P(s) + \text{others}_p \qquad (2)$$

---
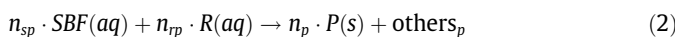
[1] Even though several ions are involved in the precipitation reaction, the net reaction may be featured by such reaction equation by properly fitting the stechiometric coefficients.

where n_{sp}, n_{rp} and n_p are the molar (stechiometric) proportions of the involved species in the precipitation reaction. Analogously to the dissolution equation (1), others$_p$ represent some other species involved in the precipitation reaction. They are neglected as well, as a first approach. Since the species involved in the precipitation reaction, Eq. (2), can diffuse through the biomaterial, one may consider that the product P may precipitate along the bulk biomaterial. However, since precipitation reactions depends on pressure, we consider, as a model hypothesis, that ideal conditions are not reached in the biomaterial interior for precipitation, being thus Eq. (2) restricted only to the biomaterial surface.

2.2. Chemical rate reaction equations

Dissolution and precipitation reactions, Eqs. (1) and (2), respectively, are expressed in terms of rate reaction equations. For the dissolution we propose a first order kinetic reaction similar to that used in previously developed models (Knabner et al., 1995; van Noorden and Pop, 2008), i.e., the formation rate of R only depends on SBF concentration such that,

$$\dot{R}_d = k_d \cdot SBF \cdot H[BG] \quad \text{in } \Omega(\mathbf{x}) \qquad (3)$$

being $\dot{\square}$ the time derivative (rate) of $\square$, k_d [1/s] the dissolution rate constant and $\Omega(\mathbf{x})$ the biomaterial domain. $H[\bullet]$ is the Heaviside function which was introduced in (3) to take into consideration the stechiometry of Eq. (1) in terms of the limiting reagent thus,

$$H[BG] = \begin{cases} 1, & BG > 0 \\ 0, & BG = 0 \end{cases} \qquad (4)$$

According to Eqs. (1) and (3), the following expression is found for the rate reaction equation of BG dissolution,

$$\dot{BG} = -\frac{n_{rd}}{n_b}\dot{R} = -\frac{n_{rd}}{n_b}k_d \cdot SBF \cdot H[BG] \quad \text{in } \Omega(\mathbf{x}) \qquad (5)$$

Likewise, using Eqs. (1) and (3) we obtain,

$$\dot{SBF}_d = -\frac{n_{rd}}{n_{sd}}\dot{R} = -\frac{n_{rd}}{n_{sd}}k_d \cdot SBF \cdot H[BG] \quad \text{in } \Omega(\mathbf{x}) \qquad (6)$$

$\dot{SBF}_d$ regarding to the SBF consumption in the dissolution equation.

On the other hand, the precipitation rate is modelled by the law of mass action kinetics, similarly to other models for the precipitation rate (van Noorden and Pop, 2008),

$$\dot{P} = k_p \cdot SBF^{n_{sp}} \cdot R^{n_{rp}} \quad \text{in } \Gamma(\mathbf{x}) \qquad (7)$$

where $k_p \left[s^{-1} \left(\frac{mol}{m^3} \right)^{1-n_{sp}-n_{rp}} \right]$ is the precipitation rate constant. Note that Eq. (7) is defined at the biomaterial surface $\Gamma(\mathbf{x})$ due to the previously introduced hypothesis that the precipitation reaction takes place at that location. The consumption rate of the reactant (R) in the precipitation reaction is obtained by using Eqs. (2) and (7) as,

$$\dot{R}_p = -\frac{n_p}{n_{rp}}\dot{P} = -\frac{n_p}{n_{rp}}k_p \cdot SBF^{n_{sp}} \cdot R^{n_{rp}} \quad \text{in } \Gamma(\mathbf{x}) \qquad (8)$$

Analogously, using Eqs. (2) and (7), the consumption rate of the SBF specie in the precipitation reaction yields:

$$\dot{SBF}_p = -\frac{n_p}{n_{sp}}\dot{P} = -\frac{n_p}{n_{sp}}k_p \cdot SBF^{n_{sp}} \cdot R^{n_{rp}} \quad \text{in } \Gamma(\mathbf{x}) \qquad (9)$$

2.3. Reaction–diffusion equations

Aqueous species are allowed to diffuse in our model as consequence of porosity and cracks developed at the interior of the biomaterial during fabrication. Diffusion is assumed to be driven by the Fick's law both for the SBF and R. Therefore, by balancing the mass transfer over an infinitesimal control volume, the following

time-dependent differential expressions are found for the *SBF* and *R*, respectively:

$$\dot{SBF} = -D_s \cdot \nabla^2[SBF] - \dot{SBF}_d \quad \text{in } \Omega(\mathbf{x}) \tag{10}$$

$$\dot{R} = -D_r \cdot \nabla^2[R] + \dot{R}_d \quad \text{in } \Omega(\mathbf{x}) \tag{11}$$

$\nabla^2[\bullet]$ being the Laplacian operator, and D_s, D_r the diffusion coefficients of *SBF* and *R*, respectively, in the biomaterial (both assumed as constant as a first approach). Using (6) in (10) it yields:

$$\dot{SBF} = -D_s \cdot \nabla^2[SBF] - \frac{n_{rd}}{n_{sd}} k_d \cdot SBF \cdot H[BG] \quad \text{in } \Omega(\mathbf{x}) \tag{12}$$

Analogously, introducing (3) in (11) we obtain,

$$\dot{R} = -D_r \cdot \nabla^2[R] + k_d \cdot SBF \cdot H[BG] \quad \text{in } \Omega(\mathbf{x}) \tag{13}$$

Ordinary differential equations (5) and (7) and reaction–diffusion equations (12) and (13) define the proposed model available to analyze bioactivity and dissolution in bioactive-glasses. Boundary conditions for Eqs. (12) and (13) are analyzed below, whereas initial conditions are defined as $BG(t = 0) = BG_0$, $P(t = 0) = 0$, $SBF(t = 0) = SBF_0$ and $R(t = 0) = 0$.

2.4. Dimensionless formulation

In order to reduce the number of parameters involved in the model, the following dimensionless variables and parameters are proposed,

$$\bar{\mathbf{x}} = \frac{\mathbf{x}}{L}; \quad \bar{t} = k_d \cdot t; \quad \overline{SBF} = \frac{SBF}{SBF_0}$$

$$\overline{BG} = \frac{BG}{SBF_0}; \quad \overline{R} = \frac{R}{SBF_0}; \quad \overline{P} = \frac{P}{SBF_0^n} \tag{14}$$

$$\overline{D}_s = \frac{D_s}{k_d L^2}; \quad \overline{D}_r = \frac{D_r}{k_d L^2}; \quad \bar{k}_p = \frac{k_p}{k_d}$$

where $\mathbf{x}$ is the vector position of a material point of the domain; L is the characteristic specimen size; $n = n_{rp} + n_{sp}$, and t is the time variable. Using the dimensionless parameters and variables according to Eq. (14), one can achieve the following set of coupled differential equations:

$$\dot{\overline{BG}} = -\frac{n_{rd}}{n_b} \cdot \overline{SBF} \cdot H[\overline{BG}] \quad \text{in } \Omega(\bar{\mathbf{x}}) \tag{15}$$

$$\dot{\overline{P}} = \bar{k}_p \cdot \overline{SBF}^{n_{sp}} \cdot \overline{R}^{n_{rp}} \quad \text{in } \Gamma(\bar{\mathbf{x}}) \tag{16}$$

$$\dot{\overline{SBF}} = -\overline{D}_s \cdot \nabla^2[\overline{SBF}] - \frac{n_{rd}}{n_{sd}} \cdot \overline{SBF} \cdot H[\overline{BG}] \quad \text{in } \Omega(\bar{\mathbf{x}}) \tag{17}$$

$$\dot{\overline{R}} = -\overline{D}_r \cdot \nabla^2[\overline{R}] + \overline{SBF} \cdot H[\overline{BG}] \quad \text{in } \Omega(\bar{\mathbf{x}}) \tag{18}$$

Hereafter, dot differentiation is referred to dimensionless time $\bar{t}$. Eqs. (15)–(18) are numerically implemented as explained in Section 3. The initial conditions for this set of equations are $\overline{BG}(\bar{t} = 0) = \overline{BG}_0$, $\overline{P}(\bar{t} = 0) = 0$, $\overline{SBF}(\bar{t} = 0) = 1$ and $\overline{R}(\bar{t} = 0) = 0$. The boundary conditions of this problem are treated in the next section.

2.5. Boundary conditions

The problem defined through the set of Eqs. (15)–(18) lacks the boundary conditions for $\overline{SBF}$ and $\overline{R}$. To define them, some simplifications are introduced. We consider that the bioactive glass is immersed in an abundant solution of SBF. Due to the reactions that take place at the boundary SBF-biomaterial, SBF concentration diminishes stechiometrically according to Eqs. (1) and (2). However, as a consequence of SBF concentration depletion, SBF diffuses along the aqueous solution. At this stage, we consider the two following assumptions: (i) SBF diffuses along the solution much more faster than in the biomaterial and it also is much more faster than

the typical reaction times, and (ii) SBF is abundant and hence no SBF depletion is considered along the solution. Therefore, we consider that SBF concentration is constant (oversaturated) along the biomaterial surface,

$$\overline{SBF}(\bar{\mathbf{x}}, \bar{t}) = 1 \quad \text{in } \Gamma(\bar{\mathbf{x}}) \tag{19}$$

This hypothesis is analogous to consider a laminar SBF flow in contact with the biomaterial (for example as in perfusion-based bioreactor experiments). In this case, this would be the actual boundary condition. Moreover, this hypothesis is enforced by the fact that SBF is usually changed or refilled at certain times through the experiment to keep a constant concentration. It should be noted that this hypothesis may not be accurate for rapid reaction times or limited amount of SBF.

To obtain the boundary conditions regarding to the reactant, a mass conservation equation is established at the SBF-biomaterial surface according to Eqs. (2), (3) (in its dimensionless form) and (16),

$$\dot{\overline{R}} = \overline{SBF} \cdot H[\overline{BG}] - \frac{n_p}{n_{rp}} \cdot \bar{k}_p \cdot \overline{SBF}^{n_{sp}} \cdot \overline{R}^{n_{rp}} \quad \text{in } \Gamma(\bar{\mathbf{x}}) \tag{20}$$

Assuming that SBF concentration is constant along the SBF-biomaterial surface according to (19), Eq. (20) is rewritten as follows:

$$\dot{\overline{R}} = H[\overline{BG}] - \frac{n_p}{n_{rp}} \bar{k}_p \cdot \overline{R}^{n_{rp}} \quad \text{in } \Gamma(\bar{\mathbf{x}}) \tag{21}$$

Here, it is noted that the biomaterial boundary $\Gamma(\bar{\mathbf{x}})$ is changing with time as a consequence of erosion and precipitation reactions on the surface (first formation silica layer and then of HA) due to the intrinsic bioactivity of the glass. We name the time $\bar{t}^\star(\bar{\mathbf{x}})$ as the instant time when a point $\bar{\mathbf{x}}$ becomes a boundary point. Therefore, the initial condition for Eq. (21) is:

$$\overline{R}(\bar{\mathbf{x}} \in \Gamma, \bar{t}^\star) = \begin{cases} 0, & \bar{t}^\star(\bar{\mathbf{x}}) = 0 \\ \overline{R}^\star, & \bar{t}^\star(\bar{\mathbf{x}}) > 0 \end{cases} \tag{22}$$

It should be noted that Eq. (22) takes into consideration a possible initial concentration of $\overline{R}$ for $\bar{t} > 0$, i.e., $\overline{R}^\star$, due to the diffusion of this substance. Eq. (21) is an ordinary differential equation which may be easily integrated.[2] Thus, the final expression of the boundary condition for the reactant reads as,

$$\overline{R}(\bar{\mathbf{x}}, \bar{t}) = \overline{R}^\star \exp[-\bar{k}_p \tau] + \frac{1}{\bar{k}_p} H[\overline{BG}](1 - \exp[-\bar{k}_p \tau]) \quad \text{in } \Gamma(\bar{\mathbf{x}}) \tag{23}$$

where $\tau = \bar{t} - \bar{t}^\star(\bar{\mathbf{x}})$.

Eq. (16) can be integrated as well, once the expression for *R* has been found in Eq. (23). It yields the following expression for *P*,

$$\overline{P}(\bar{\mathbf{x}}, \bar{t}) = H[\overline{BG}] \cdot \bar{t} - \overline{R}(\bar{\mathbf{x}}, \bar{t}) \quad \text{in } \Gamma(\bar{\mathbf{x}}) \tag{24}$$

Note that considering that the specie $\overline{P}$ is only defined at the boundary, Eq. (24) reflects the analytical solution of $\overline{P}$ once $\overline{BG}$ and $\overline{R}$ are known.

3. Numerical implementation

The developed model above through Eqs. (15), (17), (18) and (24) with initial conditions $\overline{BG}(\bar{t} = 0) = \overline{BG}_0$, $\overline{P}(\bar{t} = 0) = 0$, $\overline{SBF}(\bar{t} = 0) = 1$ and $\overline{R}(\bar{t} = 0) = 0$; and boundary conditions as in Eqs. (19) and (23), is implemented in a finite element framework. To accomplish this, the spatio-temporal discretization of the equations is developed in this section. In order to account for the dynamic generation of new boundaries and domain evolution, due

---

[2] In this case, Eq. (21) is integrated considering n_{rp}, n_p = 1 for the sake of simplicity. This value is used after for the examples of applications shown. However, Eq. (21) could be integrated for any other n_{rp}, n_p values.

to dissolution and new layer formation, i.e., bioactivity, the Voxel-FEM method is used (see Sanz-Herrera et al., 2008c; Sanz-Herrera et al., 2009b). The discretized problem and the numerical algorithms are implemented using the program Abaqus (Hibbit et al., 2001). This methodology is developed in the next subsections.

3.1. Time discretization

An implicit unconditionally stable time discretization algorithm is chosen such that $\dot{\square} = \frac{\Delta\square}{\Delta t}$ and $\square = \square^{\bar t} + \Delta\square$. Following then an incremental procedure, Eqs. (15), (17) and (18) are written, respectively, as:

$$\frac{1}{\Delta\bar{t}} \cdot \Delta\overline{BG} + \frac{n_{rd}}{n_b} \cdot \Delta\overline{SBF} \cdot H[\overline{BG} + \Delta\overline{BG}] + \frac{n_{rd}}{n_b} \cdot \overline{SBF}^{\bar t} \cdot H[\overline{BG} + \Delta\overline{BG}]$$
$$= 0 \quad \text{in } \Omega(\bar{\mathbf{x}}) \tag{25}$$

$$\frac{1}{\Delta\bar{t}} \cdot \Delta\overline{SBF} + \overline{D}_s \cdot \nabla^2[\Delta\overline{SBF}] + \frac{n_{rd}}{n_{sd}} \cdot \Delta\overline{SBF} \cdot H[\overline{BG} + \Delta\overline{BG}]$$
$$+ \overline{D}_s \cdot \nabla^2[\overline{SBF}^{\bar t}] + \frac{n_{rd}}{n_{sd}} \cdot \overline{SBF}^{\bar t} \cdot H[\overline{BG} + \Delta\overline{BG}] = 0 \quad \text{in } \Omega(\bar{\mathbf{x}}) \tag{26}$$

$$\frac{1}{\Delta\bar{t}} \cdot \Delta\overline{R} + \overline{D}_r \cdot \nabla^2[\Delta\overline{R}] - \Delta\overline{SBF} \cdot H[\overline{BG} + \Delta\overline{BG}] + \overline{D}_r \cdot \nabla^2[\overline{R}^{\bar t}]$$
$$- \overline{SBF}^{\bar t} \cdot H[\overline{BG} + \Delta\overline{BG}] = 0 \quad \text{in } \Omega(\bar{\mathbf{x}}) \tag{27}$$

For convenience, boundary conditions, defined through Eqs. (23) and (24), are expressed, respectively in an incremental fashion,

$$\Delta\overline{R} = \overline{R}^{\bar t} + \frac{1}{\bar{k}_p} H[\overline{BG} + \Delta\overline{BG}]$$
$$+ \exp[-\bar{k}_p \cdot \Delta\bar{t}]\left(\overline{R}^{\bar t} - \frac{1}{\bar{k}_p} H[\overline{BG} + \Delta\overline{BG}]\right) \quad \text{in } \Gamma(\bar{\mathbf{x}}) \tag{28}$$

$$\Delta\overline{P} = \Delta\bar{t} - \Delta\overline{R} \quad \text{in } \Gamma(\bar{\mathbf{x}}) \tag{29}$$

Differential equations (26) and (27) are now spatially discretized using a finite element framework. This procedure is explained in the next section.

3.2. Spatial finite element discretization

Incremental variables $\Delta\overline{SBF}$ and $\Delta\overline{R}$ are interpolated over a finite element through a nodal (discrete) values, such that, $\Delta\overline{SBF}(\mathbf{x}) \approx \mathbf{N}_s(\mathbf{x}) \cdot \Delta\overline{SBF}$ and $\Delta\overline{R}(\mathbf{x}) \approx \mathbf{N}_r(\mathbf{x}) \cdot \Delta\overline{R}$. Interpolating shape functions are assumed as $\mathbf{N} = \mathbf{N}_s = \mathbf{N}_r$, whilst $\Delta\overline{SBF}$ and $\Delta\overline{R}$ are a discrete node-valued vectors containing $\Delta\overline{SBF}$ and $\Delta\overline{R}$ at the position of each node of the element, respectively. Therefore, using this finite element discretization (see additionally Bathe, 1996; Hughes, 2000; Reddy, 1993; Zienkiewicz and Taylor, 2000), the weak form of Eq. (26) yields,

$$\mathbb{A}_{e=1}^{N_{el}}\left\{\frac{1}{\Delta\bar{t}} \int_{\Omega_e} \mathbf{N}^T \cdot \mathbf{N} \cdot d\Omega_e \cdot \Delta\overline{SBF} + \int_{\Omega_e} \mathbf{B}^T \cdot \overline{D}_s \cdot \mathbf{B} \cdot d\Omega_e \cdot \Delta\overline{SBF}\right.$$
$$+ \int_{\Omega_e} \frac{n_{rd}}{n_{sd}} \cdot \mathbf{N}^T \cdot \mathbf{N} \cdot d\Omega_e \cdot \mathbf{I} \cdot H[\overline{BG} + \Delta\overline{BG}] \cdot \Delta\overline{SBF}$$
$$+ \int_{\Omega_e} \mathbf{B}^T \cdot \overline{D}_s \cdot \mathbf{B} \cdot d\Omega_e \cdot \overline{SBF}^{\bar t} + \int_{\Omega_e} \frac{n_{rd}}{n_{sd}} \cdot \mathbf{N}^T \cdot \mathbf{N} \cdot d\Omega_e \cdot \mathbf{I}$$
$$\left. \cdot H[\overline{BG} + \Delta\overline{BG}] \cdot \overline{SBF}^{\bar t}\right\} = \mathbf{0} \tag{30}$$

$\mathbf{B}$ being the shape function gradient matrix and $\mathbf{I}$ the unity matrix with dimension of the vector $\Delta\overline{SBF}$. The symbol $\mathbb{A}$ represents the assembly operator and N_{el} the number of elements.

Eq. (30) is now developed for a single element as,

$$\left(\frac{1}{\Delta\bar{t}} \cdot \mathbf{M}_s + \mathbf{K}_s + \frac{n_{rd}}{n_{sd}}\mathbf{M}_s \cdot \mathbf{I} \cdot H[\overline{BG} + \Delta\overline{BG}]\right) \cdot \Delta\overline{SBF}$$
$$+ \left(\mathbf{K}_s + \frac{n_{rd}}{n_{sd}}\mathbf{M}_s \cdot \mathbf{I} \cdot H[\overline{BG} + \Delta\overline{BG}]\right) \cdot \overline{SBF}^{\bar t} = \mathbf{0} \tag{31}$$

$\mathbf{M}_s$ and $\mathbf{K}_s$ are the standard mass and stiffness matrices of Eq. (30), respectively (see Bathe, 1996; Hughes, 2000; Reddy, 1993; Zienkiewicz and Taylor, 2000). Furthermore, Eq. (31) can be additionally rewritten and expressed as,

$$\widetilde{\mathbf{K}}_s(\overline{BG}) \cdot \Delta\overline{SBF} = \mathscr{R}_s^{\bar t}(\overline{BG}) \tag{32}$$

$\widetilde{\mathbf{K}}_s$ being the extended stiffness matrix which may be found by matching Eqs. (31) and (32). Eq. (32) is arranged taking the unknown values at the left hand side and the residual values, i.e., those known from the previous increment at the right hand side in the residual vector $\mathcal{R}_s^{\bar t}$. Both the extended stiffness matrix and residual vector depend upon the $\overline{BG}$ values. The treatment of this non-linearity is easily circumvented as explained below.

Analogously, Eq. (27) can be developed once introduced the spatial (nodal) discretization above, and establishing Eq. (27) in its weak form, namely,

$$\mathbb{A}_{e=1}^{N_{el}}\left\{\frac{1}{\Delta\bar{t}} \int_{\Omega_e} \mathbf{N}^T \cdot \mathbf{N} \cdot d\Omega_e \cdot \Delta\overline{R} + \int_{\Omega_e} \mathbf{B}^T \cdot \overline{D}_r \cdot \mathbf{B} \cdot d\Omega_e \cdot \Delta\overline{R}\right.$$
$$- \int_{\Omega_e} \mathbf{N}^T \cdot \mathbf{N} \cdot d\Omega_e \cdot \mathbf{I} \cdot H[\overline{BG} + \Delta\overline{BG}] \cdot \Delta\overline{SBF}$$
$$\left. + \int_{\Omega_e} \mathbf{B}^T \cdot \overline{D}_r \cdot \mathbf{B} \cdot d\Omega_e \cdot \overline{R}^{\bar t} - \int_{\Omega_e} \mathbf{N}^T \cdot \mathbf{N} \cdot d\Omega_e \cdot \mathbf{I} \cdot H[\overline{BG} + \Delta\overline{BG}] \cdot \overline{R}^{\bar t}\right\} = \mathbf{0} \tag{33}$$

Furthermore, Eq. (33) can be written for one element in terms of the mass and stiffness matrices as,

$$\left(\frac{1}{\Delta\bar{t}} \cdot \mathbf{M}_r + \mathbf{K}_r\right) \cdot \Delta\overline{R} - \mathbf{M}_r \cdot \mathbf{I} \cdot H[\overline{BG} + \Delta\overline{BG}] \cdot \Delta\overline{SBF}$$
$$+ \left(\mathbf{K}_r - \mathbf{M}_r \cdot \mathbf{I} \cdot H[\overline{BG} + \Delta\overline{BG}]\right) \cdot \overline{R}^{\bar t} = \mathbf{0} \tag{34}$$

Finally, Eq. (34) is expressed in terms of the unknown (left hand side) and known residual (right hand side) values,

$$\widetilde{\mathbf{K}}_r \cdot \Delta\overline{R} - \widetilde{\mathbf{M}}_r(\overline{BG}) \cdot \Delta\overline{SBF} = \mathcal{R}_r^{\bar t}(\overline{BG}) \tag{35}$$

Again, matrices $\widetilde{\mathbf{K}}_r$, $\widetilde{\mathbf{M}}_r$ and residual vector $\mathcal{R}_r^{\bar t}$ are a function of variable $\overline{BG}$. Eqs. (32) and (35) are arranged in the following set of linearized algebraic system of equations as,

$$\begin{bmatrix} \widetilde{\mathbf{K}}_s(\overline{BG}) & \mathbf{0} \\ -\widetilde{\mathbf{M}}_r(\overline{BG}) & \widetilde{\mathbf{K}}_r \end{bmatrix} \left\{\begin{array}{c} \Delta\overline{SBF} \\ \Delta\mathbf{R} \end{array}\right\} = \left\{\begin{array}{c} \mathcal{R}_s^{\bar t}(\overline{BG}) \\ \mathcal{R}_r^{\bar t}(\overline{BG}) \end{array}\right\} \tag{36}$$

The solution procedure to solve the proposed model is summarized in the following algorithm:

1. Initialize variables with nodal values $\overline{SBF}(\bar{t} = 0) = \mathbf{1}$, $\overline{BG}(\bar{t} = 0) = \overline{BG}_0 \cdot \mathbf{1}$ (assuming homogeneous distribution), $\overline{\mathbf{P}}(\bar{t} = 0) = \mathbf{0}$, $\overline{\mathbf{R}}(\bar{t} = 0) = \mathbf{0}$, being $\mathbf{0}$ and $\mathbf{1}$ a vectors with the dimension of $\overline{SBF}$ containing 0 and 1 at every row, respectively.
2. Impose boundary conditions at $\bar{t} + \Delta\bar{t}$ for variables $\overline{SBF}$ and $\overline{R}$, such that, $\overline{SBF} = \mathbf{1}$ and $\overline{\mathbf{R}} = \Delta\overline{\mathbf{R}} + \overline{\mathbf{R}}^{\bar t}$, being $\Delta\overline{\mathbf{R}}$ computed through Eq. (28).
3. Compute the system defined by Eq. (36) for each element and assembly to obtain the whole global algebraic system. Consider $H[\overline{BG} + \Delta\overline{BG}] = \mathbf{1}$. This step yields the solution for $\Delta\overline{SBF}$ and $\Delta\overline{R}$.
4. Once computed these incremental quantities, $\Delta\overline{BG}$ and $\Delta\overline{\mathbf{P}}$ are obtained using Eqs. (25) and (29), respectively. Variable values at current increment are obtained as $\square = \square^{\bar t} + \Delta\square$.
5. If $\overline{SBF}$ becomes negative for the component i of the vector, then GO TO item (3) considering now $H_i[\overline{BG} + \Delta\overline{BG}] = 0$.

Thus the process of dissolution and new layer formation is explicitly modelled in the present work to simulate the geometry evolution with time. This is accomplished by means of the Voxel-FEM and explained in the next section.

3.3. Voxel-FEM methodology

Geometry evolution, i.e., dissolution and new layer formation, is here simulated by means of the Voxel-FEM method (Adachi et al., 2001; Guldberg et al., 1998). Briefly, each finite element is considered to be a voxel analogously to a straight edge eight-noded hexahedron with linear interpolation. Due to the characteristic features of this kind of element, mass and stiffness matrices can be analytically derived, and the assembly process is speeded up by binary matrix transformations (Sanz-Herrera, 2008a; Sanz-Herrera et al., 2008c). Moreover, the dissolution process, i.e., disappearance, and new layer formation can be easily simulated by removing and adding voxels, respectively. In contrast, this method becomes problematic when Neumann boundary conditions are imposed (this is not the case in our problem) and provides a poor approximation of the geometry when the mesh is relatively coarse (Sanz-Herrera, 2008a).

Voxel linear shape functions are defined in natural coordinates as,

$$N = \frac{1}{8}(1 \pm \xi)(1 \pm \eta)(1 \pm \varsigma) \tag{37}$$

being $\xi, \eta, \varsigma \in [-1, 1]$. The sign of each coordinate is taken according to the proper nodal location (eight functions in total). Therefore, mass matrices expressed above can be obtained as follows:

$$\mathbf{M}_i = \int_{\Omega_e} \mathbf{N}^T \cdot \mathbf{N} \cdot d\Omega_e = \int_{-1}^{1} \int_{-1}^{1} \int_{-1}^{1} \mathbf{N}^T \cdot \mathbf{N} \cdot a^3 \cdot d\xi \, d\eta \, d\varsigma \tag{38}$$

a being the semivoxel length and $i = s, r$. Analogously, using shape functions as in Eq. (37), stiffness matrices are written as,

$$\mathbf{K}_i = \int_{\Omega_e} \overline{D}_i \cdot \nabla \mathbf{N}^T \cdot \nabla \mathbf{N} \cdot d\Omega_e$$
$$= \int_{-1}^{1} \int_{-1}^{1} \int_{-1}^{1} \overline{D}_i \cdot \nabla \mathbf{N}^T \cdot \nabla \mathbf{N} \cdot a \cdot d\xi d\eta d\varsigma \tag{39}$$

The above mass (Eq. (38)) and stiffness (Eq. (39)) matrices may be analytically integrated. They are expressed in their closed form in Tables 1 and 2, respectively.

The solution of the established problem joined with its numerical implementation by the Voxel-FEM, explained above, yield the variables involved at each node of the voxel mesh. Thus, dissolution and precipitation are easily simulated by removing and adding voxels, respectively. For that purpose, we use an internal third order binary mesh featured by subscripts i, j, k, with $i, j, k = 1, \ldots$ voxlength, being voxlength the voxel resolution. This matrix contains

Table 1
Matrix components M_{mn} of Eq. (38).

m	n							
	1	2	3	4	5	6	7	8
1	$\frac{8a^3}{27}$	$\frac{4a^3}{27}$	$\frac{2a^3}{27}$	$\frac{4a^3}{27}$	$\frac{4a^3}{27}$	$\frac{2a^3}{27}$	$\frac{a^3}{27}$	$\frac{2a^3}{27}$
2		$\frac{8a^3}{27}$	$\frac{4a^3}{27}$	$\frac{2a^3}{27}$	$\frac{2a^3}{27}$	$\frac{4a^3}{27}$	$\frac{2a^3}{27}$	$\frac{a^3}{27}$
3			$\frac{8a^3}{27}$	$\frac{4a^3}{27}$	$\frac{a^3}{27}$	$\frac{2a^3}{27}$	$\frac{4a^3}{27}$	$\frac{2a^3}{27}$
4				$\frac{8a^3}{27}$	$\frac{2a^3}{27}$	$\frac{a^3}{27}$	$\frac{2a^3}{27}$	$\frac{4a^3}{27}$
5					$\frac{8a^3}{27}$	$\frac{4a^3}{27}$	$\frac{2a^3}{27}$	$\frac{4a^3}{27}$
6		Symmetric				$\frac{8a^3}{27}$	$\frac{4a^3}{27}$	$\frac{2a^3}{27}$
7							$\frac{8a^3}{27}$	$\frac{4a^3}{27}$
8								$\frac{8a^3}{27}$

Table 2
Matrix components K_{mn} of Eq. (39).

m	n							
	1	2	3	4	5	6	7	8
1	$\frac{2a\overline{D}_i}{3}$	0	$\frac{-(a\overline{D}_i)}{6}$	0	0	$\frac{-(a\overline{D}_i)}{6}$	$\frac{-(a\overline{D}_i)}{6}$	$\frac{-(a\overline{D}_i)}{6}$
2		$\frac{2a\overline{D}_i}{3}$	0	$\frac{-(a\overline{D}_i)}{6}$	$\frac{-(a\overline{D}_i)}{6}$	0	$\frac{-(a\overline{D}_i)}{6}$	$\frac{-(a\overline{D}_i)}{6}$
3			$\frac{2a\overline{D}_i}{3}$	0	$\frac{-(a\overline{D}_i)}{6}$	$\frac{-(a\overline{D}_i)}{6}$	0	$\frac{-(a\overline{D}_i)}{6}$
4				$\frac{2a\overline{D}_i}{3}$	$\frac{-(a\overline{D}_i)}{6}$	$\frac{-(a\overline{D}_i)}{6}$	$\frac{-(a\overline{D}_i)}{6}$	0
5					$\frac{2a\overline{D}_i}{3}$	0	$\frac{-(a\overline{D}_i)}{6}$	0
6		Symmetric				$\frac{2a\overline{D}_i}{3}$	0	$\frac{-(a\overline{D}_i)}{6}$
7							$\frac{2a\overline{D}_i}{3}$	0
8								$\frac{2a\overline{D}_i}{3}$

1 if the region of the space located at i, j, k is occupied by a voxel, being null otherwise. The dissolution (disappearance) algorithm proceeds as follows (see additionally Fig. 2 and Sanz-Herrera et al., 2008c):

1. Identify boundary voxels in the binary matrix mesh.
2. Compute BG concentration at boundary voxel centroids by means of a Lagrangian interpolation.
3. If $BG < BG_{cr}$, being BG_{cr} a model parameter, then remove the boundary voxel.

On the other hand, the algorithm available to simulate the precipitation phenomenon is analogously established (see Fig. 3 and Sanz-Herrera et al., 2008c),

1. Identify potential voxel candidates to shift into precipitate (layer) voxels. These are either the boundary voxel (equal to 1 in the binary matrix mesh) or the adjacent ones to the boundary voxels (equal to 0 in the binary matrix mesh).
2. Compute product concentration P at voxel candidate centroids through a Lagrangian interpolation.
3. If $P > P_{cr}$ and $BG < BG_{cr}$ (note that $BG = 0$ in adjacent voxels), being P_{cr} a model parameter, then shift the candidate voxel into a precipitate voxel.
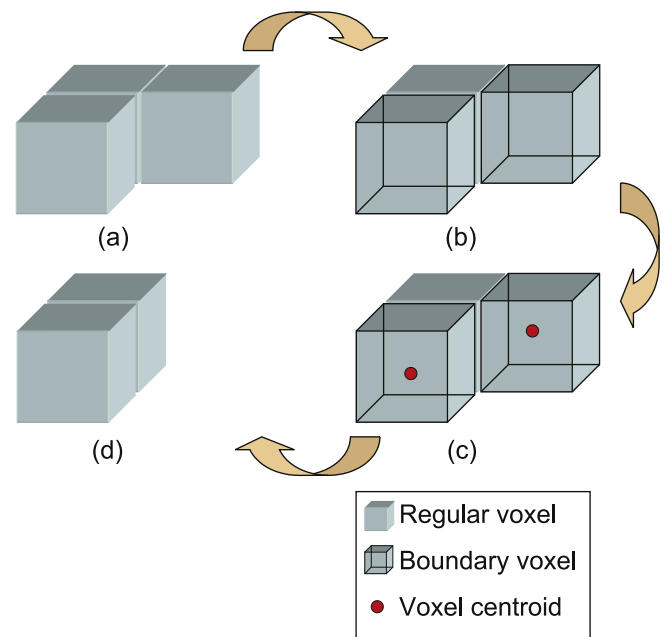

Fig. 2. Dissolution scheme: (a) initial voxel mesh, (b) identify boundary voxels, (c) compute BG at boundary voxels centroids and (d) if $BG < BG_{cr}$ then remove the boundary voxel.
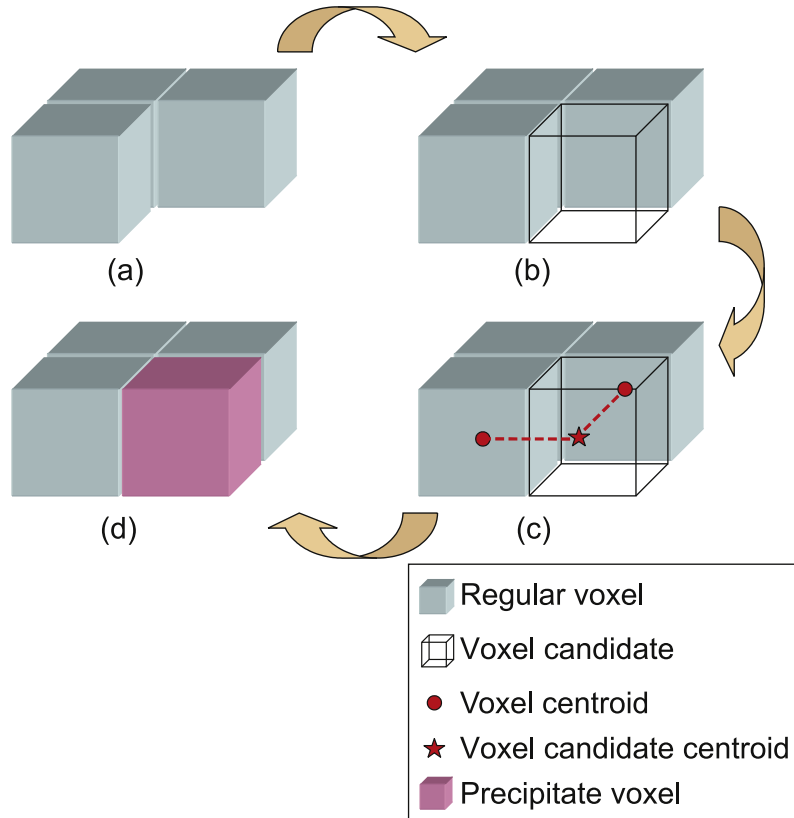
Fig. 3. Precipitation scheme: (a) initial voxel mesh, (b) identify voxel candidate, (c) compute precipitate concentration P at voxel candidates and (d) add a new precipitate voxel if $P > P_{cr}$ at voxel candidate centroid.

4. Results

In this section, some examples of applications of the model proposed above are shown. For that purpose, we consider a bioactive glass scaffold with a certain microstructure immersed in an infinite SBF medium.

A priori, any bioactive material may be analyzed just fitting the model parameters, namely, n_{sd}, n_b, n_{rd}, n_{sp}, n_{rp}, n_p, $\bar{k}_p$, $\overline{D}_s$ and $\overline{D}_r$. Molar coefficients n_{sd}, n_b, n_{rd}, n_{sp}, n_{rp} and n_p may be obtained by analyzing the chemical reagents involved in the reactions, whereas $\bar{k}_p$ is determined measuring the amount of formed product P per time. On the other hand, diffusion coefficients $\overline{D}_s$ and $\overline{D}_r$ can be determined by the setup of Fickean experiments for the SBF and reactant, respectively, within the biomaterial. Obtaining model parameters requires experimental setup for each specific biomaterial. However, these tests regard to well-established standard protocols. As a first simplified approach, we consider $n_{sd} = n_b = n_{rd} = n_{sp} = n_{rp} = n_p = 1$ due to the difficulty to search this specific information in the literature. Furthermore, we assume that the diffusion velocity of SBF within the biomaterial is the same than the reactant, such that, $\overline{D}_s = \overline{D}_r$. On the other hand, we assume the formed HA layer to be impermeable and therefore null diffusion in this part of the domain occurs. Note that according to these simplifications, the model is driven by parameters $\bar{k}_p$ and $\overline{D}_s = \overline{D}_r = \overline{D}$. Since the aim of the paper is not an exhaustive model validation, the chosen parameters were not specifically related to known practical conditions.

In the first example, a sensitivity analysis to model parameters $\bar{k}_p$ and $\overline{D}$ is performed. A generic microstructure is considered in this case. Secondly, an actual Bioglass® scaffold microstructure is reproduced in order to simulate a realistic example of dissolution and bioactivity. Results are discussed, to some extent, based on qualitative validation of the model.

4.1. Example of application: parametric analysis

Fig. 4 represents the microstructure of 1/8 of a spheric biomaterial (scaffold) containing a hole. This kind of microarchitecture is usually found in scaffolds fabricated by means of a porogens (Diego
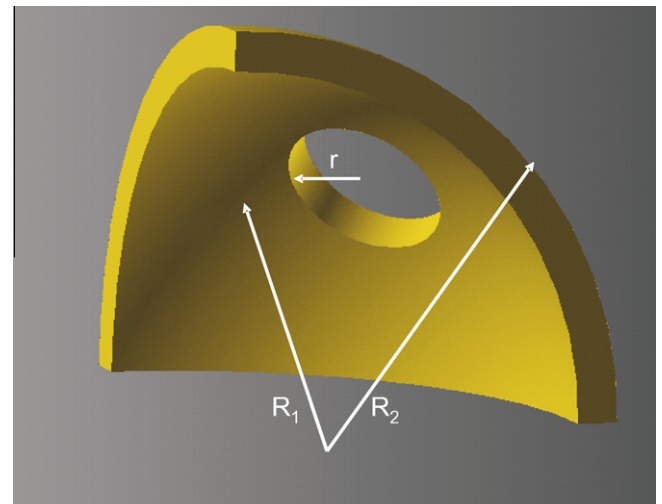

Fig. 4. Problem geometry for the parametric analysis, 1/8 of a spheric biomaterial (scaffold) wall containing a hole.
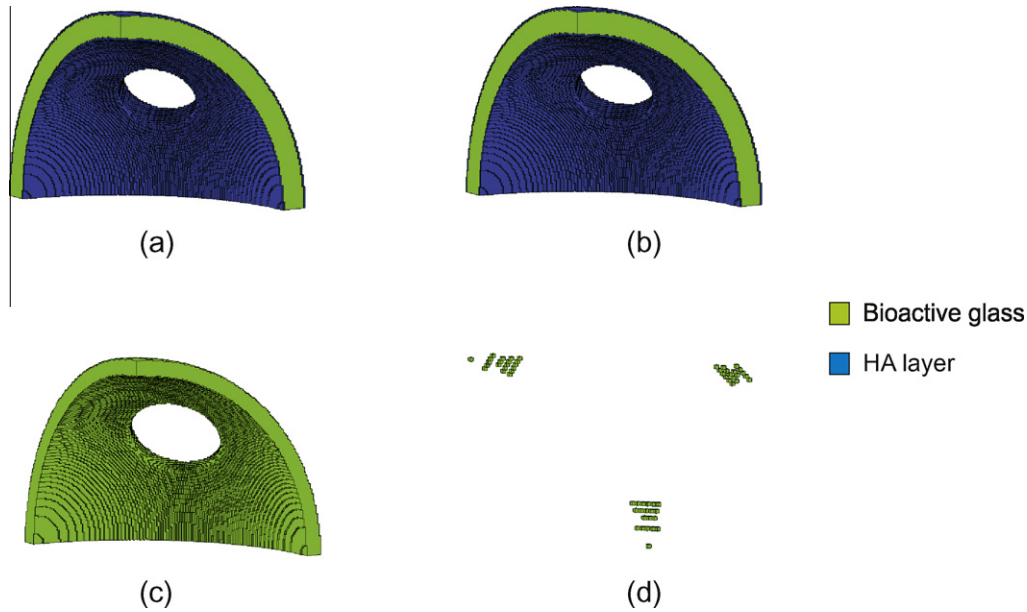
Fig. 5. Geometry of the specimen at the final stage of the analysis. (a) Case i at $\bar{t} = 20$, (b) case ii at $\bar{t} = 20$, (c) case iii at $\bar{t} = 20$ and (d) case iv at $\bar{t} = 19$.

et al., 2007). Symmetric boundary conditions are applied on the symmetry planes, whereas the biomaterial is assumed to be inmmersed in SBF. Geometric aspect ratios are $R_2/R_1 = 10/9$, $R_2/r = 5$, with initial species concentration $\overline{SBF}_0 = 1$, $\overline{BG}_0 = 1$. The rest of parameters are set to $\overline{BG}_{cr} = 0.5$ and $\overline{P}_{cr} = 0.4$.

Four different cases are analyzed with different parameters, namely:

- Case i: $\overline{D} = 0.0004$, $\bar{k}_p = 6.0$.
- Case ii: $\overline{D} = 0.004$, $\bar{k}_p = 6.0$.
- Case iii: $\overline{D} = 0.0004$, $\bar{k}_p = 3.0$.
- Case iv: $\overline{D} = 0.004$, $\bar{k}_p = 3.0$.

The selected cases correspond to the analysis of the most important model parameters for bioactivity and biomaterial degradation. Dimensionless diffusion parameter $\overline{D}$ regards to aqueous species transport within the biomaterial which may be tailored, to some extent, controlling biomaterial microporosity and cracks formation during scaffold fabrication. On the other hand, dimensionless precipitation rate constant $\bar{k}_p$ regards to precipitation deposition velocity on the surface, which is an important parameter dependent on glass composition.

Fig. 5 shows the geometry of the specimen at the final stage of the analysis for each case. We can qualitatively observe both the macroscopic dissolution and the formation of the HA layer for cases i and ii. The effect of diffusion and precipitation velocity parameters can be easily understood in the model: a rapid precipitation velocity yields to HA layer formation (cases i and ii) even in the case that diffusion is slow (case i). This is true up to a sufficiently high value of $\overline{D}$ such that the structure starts degrading before HA formation.

Furthermore, slow values of k_p result in no HA layer and consequently biomaterial dissolution (case iii). The higher the velocity of dissolution is in this case, the quicker dissolution we get as shown in case iv (see additionally the animation in the supplementary material for the dissolution evolution in case iv). The obtained results in Fig. 5 are in agreement with the experimental trends (Chen et al., 2006a). It is observed that a slow dissolution rate slows down the precipitation phenomenon due to the lack of released ions to the surrounding SBF (Tilocca, 2009). On the other hand, a rapid

HA formation must reflect a fast dissolution of the glass network (Tilocca, 2009), as predicted numerically.

In order to account for degradation and precipitate formation, two indicators are defined over the volume, namely,

$$DEG(\%) = 100 \cdot \left(\overline{BG}_0 - \frac{1}{V_0} \int_{V_0} \overline{BG}(\bar{t}) dV_0 \right) \tag{40}$$

$$PREC(\%) = 100 \cdot \left(\frac{1}{V_0} \int_{V_0} \overline{P}(\bar{t}) \, dV_0 + \frac{V_{HA}(\bar{t})}{V_0} \right) \tag{41}$$

V_0 being the initial glass volume and V_{HA} the HA layer volume formed during precipitation. Finally the mass loss is defined as,

$$ML(\%) = DEG - PREC \tag{42}$$

Fig. 6 plots the degradation evolution for the different cases computed through Eq. (40). Note that, only cases i and ii develop a HA layer on the boundary (see Fig. 5) starting from time equal
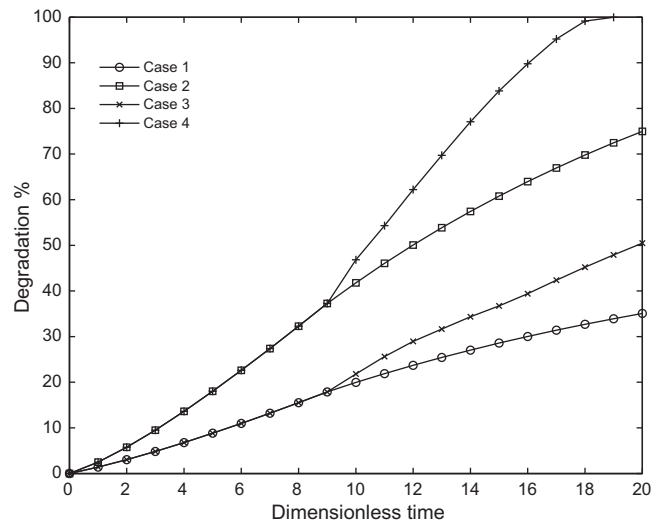

Fig. 6. Overall degradation in the specimen computed through Eq. (40) for the different analyzed cases.
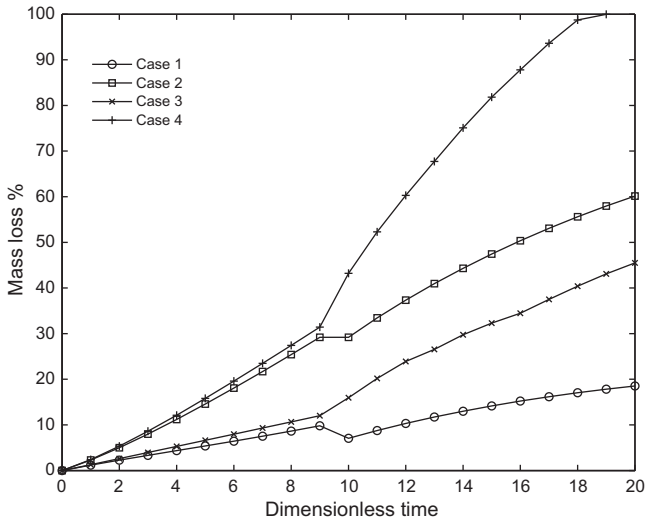
Fig. 7. Overall mass loss in the specimen computed through Eq. (42) for the different analyzed cases.

to 9. Therefore, it can be observed in Fig. 6 that cases were HA layer was formed prevented, or slowed down, the degradation process since time equal to 9. Therefore, HA layer tends to passivate the bioglass surface against further dissolution. This fact has been largely observed experimentally (see for instance Guarino et al., 2007; Kokubo et al., 1990; Tilocca, 2009). On the other hand, cases iii and iv (no HA is formed) promoted and speeded up degradation starting from time equal to 10, which is the time when $\overline{BG}$ reaches the critical value at boundary voxels, and voxels start to disappear. The difference of behaviors for the different parameters explained above, are also reproduced in Fig. 6. In Fig. 7 the total mass loss of the specimen by computation of Eq. (42) is shown. It can be observed for the different cases the effect of precipitation and new HA formation on degradation. Depending on the rate of degradation, new mass formation can slow down or even temporary reverse the trend as for example in case i, which has been also experimentally observed (Bil et al., 2007; Boccaccini et al., 2007; Roether et al., 2002a).

Note that an excessively fast degradation rate joined to a slow precipitation velocity (case iv) yields the complete disappearance of the biomaterial before the analysis is ended.

4.2. Actual Bioglass® scaffold microstructure

Here an actual Bioglass® scaffold microstructure is simulated (see Fig. 8). A unit cell with dimensions $1 \times 1 \times 1$ was chosen from
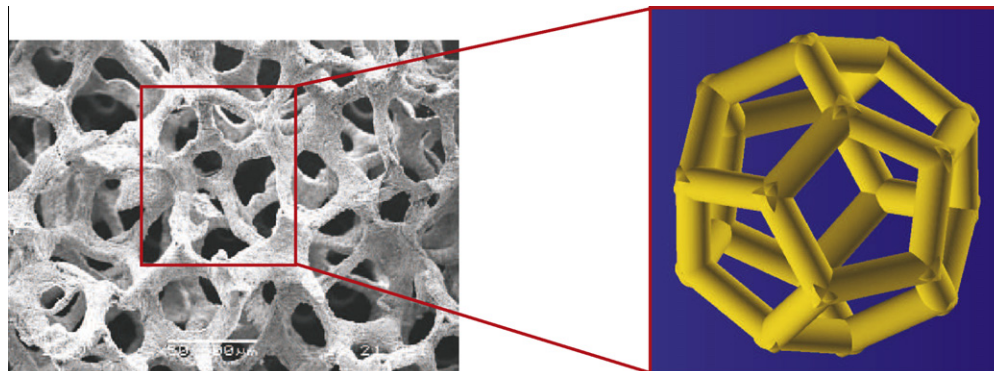
the actual geometry to simulate bioactivity and biomaterial dissolution. This unit cell results in a pentagonal dodecahedron with aspect ratio $R/r = 8.66$ being R the radius of the containing sphere in the unit cell and r the radius of the rods of the dodecahedron. Geometric relationships and characterisation of the biomaterial can be seen in Chen et al. (2006a) and Chen and Boccaccini (2006b). For the simulation of the problem using the proposed model, we select the parameters of case i of the problem above. Fig. 9 shows the geometry evolution with dimensionless time $\bar{t}$ of the problem stated in Fig. 8. As consequence of degradation, ion release and precipitation, the HA layer is formed in the geometry around dimensionless time $\bar{t} = 9$. The thickness and distribution of the HA layer can be observed in Fig. 9 for different cross sections of the geometry at different times.

Results regarding $\overline{SBF}$, $\overline{BG}$, $\overline{R}$ and $\overline{P}$ concentrations are shown in Figs. 10–13, respectively.

Fig. 10 highlights the $\overline{SBF}$ distribution in the Bioglass® interior. At the beginning ($\bar{t} = 1$) the body fluid concentrates preferentially
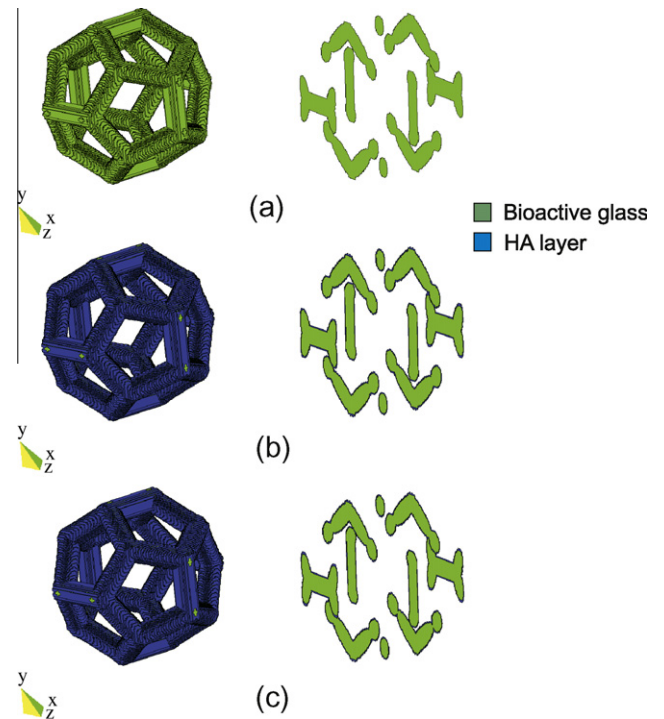

Fig. 9. Left: Geometry evolution of the unit cell Bioglass® scaffold (see also Fig. 8). Right: Equally spaced sections of the geometry presented in the left along the x-axis. (a) $\bar{t} = 1$, (b) $\bar{t} = 10$ and (c) $\bar{t} = 20$. Containing unit cell sphere diameter 800 µm.
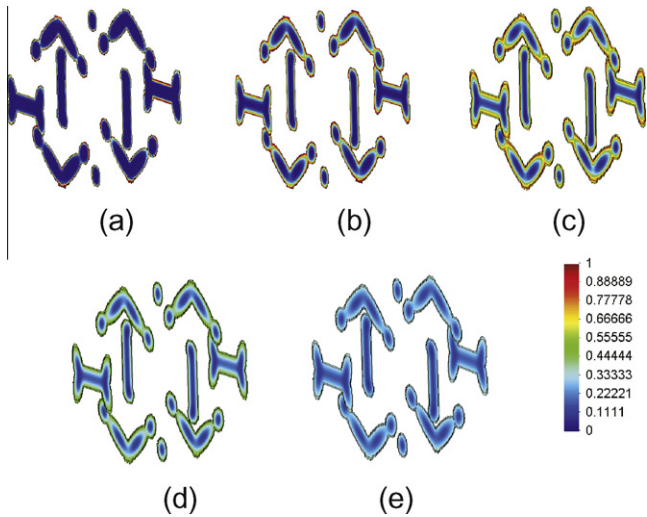

Fig. 8. Actual Bioglass® scaffold microstructure (left) taken from Chen and Boccaccini (2006b) and unit cell model (right). Containing unit cell sphere diameter 800 µm.

Fig. 10. $\overline{SBF}$ concentration at the different sections (see Fig. 9). (a) $\bar{t} = 1$, (b) $\bar{t} = 5$, (c) $\bar{t} = 10$, (d) $\bar{t} = 15$, (e) $\bar{t} = 20$. Containing unit cell sphere diameter 800 μm.
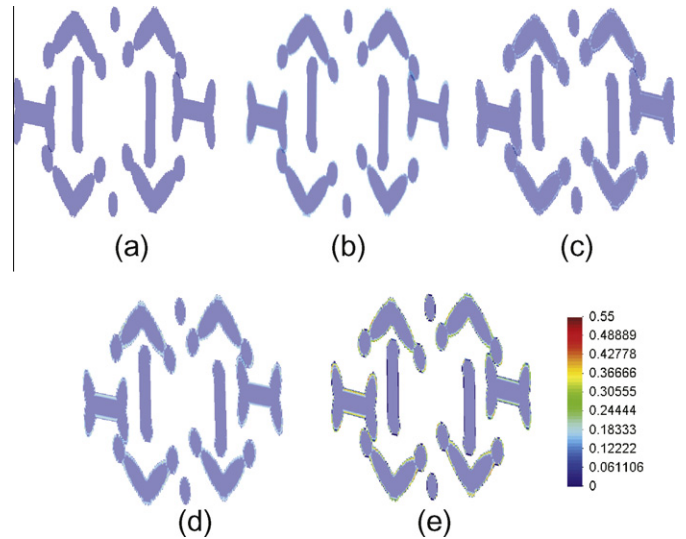

Fig. 13. $\overline{P}$ concentration at the different sections (see Fig. 9). (a) $\bar{t} = 1$, (b) $\bar{t} = 5$, (c) $\bar{t} = 10$, (d) $\bar{t} = 15$, (e) $\bar{t} = 20$. Containing unit cell sphere diameter 800 μm.

Fig. 11. $\overline{BG}$ concentration at the different sections (see Fig. 9). (a) $\bar{t} = 1$, (b) $\bar{t} = 5$, (c) $\bar{t} = 10$, (d) $\bar{t} = 15$, (e) $\bar{t} = 20$. Containing unit cell sphere diameter 800 μm.
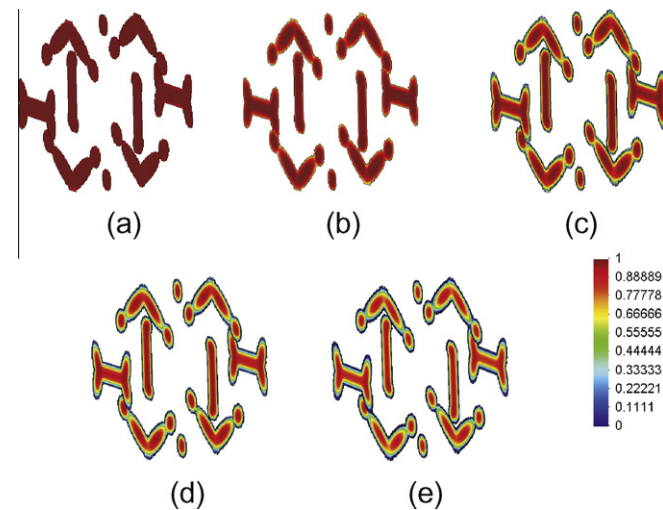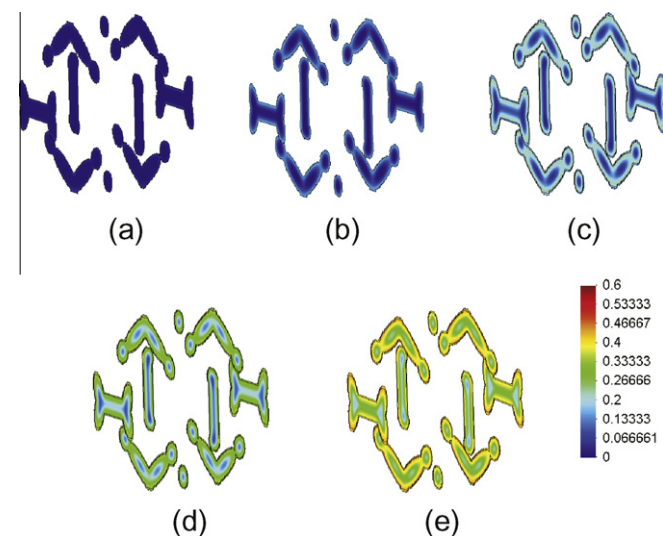
at the boundary, and increases with time in the interior due to diffusion. Once the HA layer is formed, the body fluid concentration is depleted due to the impermeable condition of the layer.

On the other hand, Fig. 11 shows the $\overline{BG}$ concentration with time. This field decreases with time as a consequence of $\overline{SBF}$ diffusion, being thus a complementary behavior to $\overline{SBF}$. Furthermore, the evolution of the reaction product $\overline{R}$ is drawn in Fig. 12. Note the increasing trend of $\overline{R}$ with time due to ion release by $\overline{BG}$ dissolution and $\overline{SBF}$ diffusion. Finally, the precipitate concentration (only at the boundary where this variable is defined) can be seen in Fig. 13. An increasing trend with time is observed due to ion release, SBF diffusion and reactant circulation to the boundary.

Fig. 14 shows both the degradation and mass loss in the whole unit cell of the Bioglass® scaffold versus time. These variables were computed through Eqs. (40) and (42), respectively. A similar trend, in this example, is observed as in the case (i) of the previous section. Here, the degradation slope changes once the HA layer is

Fig. 12. $\overline{R}$ concentration at the different sections (see Fig. 9). (a) $\bar{t} = 1$, (b) $\bar{t} = 5$, (c) $\bar{t} = 10$, (d) $\bar{t} = 15$, (e) $\bar{t} = 20$. Containing unit cell sphere diameter 800 μm.
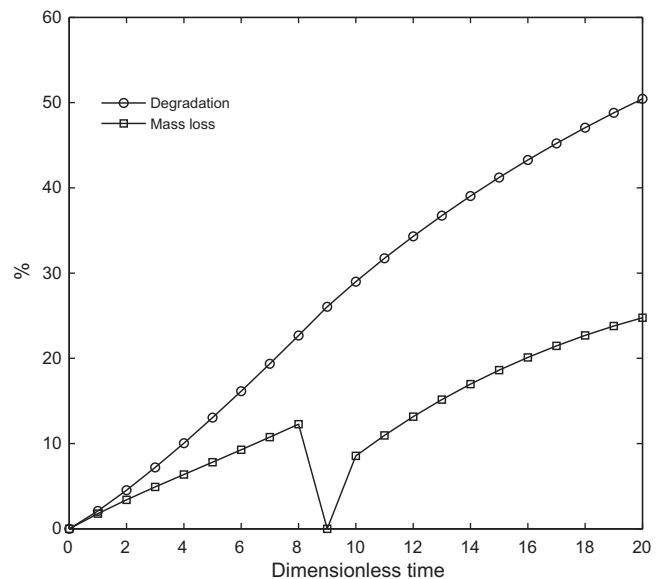

Fig. 14. Overall degradation and mass loss in the specimen computed through Eqs. (40) and (42), respectively, for the actual Bioglass® scaffold.

formed on the scaffold boundary (around time equal to 9). After this effect, degradation slows down as a consequence of the impermeable layer. Moreover, mass loss increases up to a time when it abruptly decays due to the formation of the HA layer. Once the layer is formed, it recovers the precipitate formation trend, as expected from experimental evidence (Tilocca, 2009).

5. Conclusions

A novel biodegradation model suitable for the macroscopic simulation of bioactivity and dissolution of bioactive glasses has been proposed. The model is posed at the continuum level and is rationally based on the most fundamental chemical equations, identifying four main generic species involved in the phenomenon of bioactivity and glass dissolution. Many other ions and species are involved, in this complex process of bioactive glass surface reactions in SBF which were neglected in our model. However, the model may be easily extended considering such species in two ways: first, one can write dissolution and precipitation Eqs. (1) and (2), respectively, considering a number of different species. The kinetics of each species must be also modelled and each one included in the global model as an independent variable. Therefore, the number of parameters to be fitted and model variables increases. The second simplified approach to consider the neglected ionic species, as a rough approach, is to fit an average molar content and average kinetic equation, to account for them through the stechiometric coefficients of the variable $others_d$ and $others_p$ in Eqs. (1) and (2), respectively. Variables $others_d$ and $others_p$ should be then incorporated in the global model.

Biomaterial structure evolution, as consequence of both dissolution and HA layer formation (as a measure of bioactivity), has been simulated using the Voxel-FEM. Other geometric methods based on the level set or isogeometric analysis may be explored in order to get a better representation of the geometry rather than the Voxel-FEM. However, this method provides a robust and efficient platform to simulate structure evolution of complex geometries.

Once the model here presented is properly validated, it may serve as a useful platform for designing protocols to test biodegradation and bioactivity of Bioglass®-based scaffolds, which are an active and promising area of research of biomaterials for bone tissue engineering and regenerative medicine fields.

Acknowledgements

Appendix A. Supplementary data

Supplementary data associated with this article can be found, in the online version, at doi:10.1016/j.ijsolstr.2010.09.025.

References

Adachi, T., Tsubota, K.I., Tomita, Y., Hollister, S.J., 2001. Trabecular surface remodeling simulation for cancellous bone using microstructural voxel finite element models. J. Biomech. Eng. – Trans. ASME 123, 403–409.
Adachi, T., Osako, Y., Tanaka, M., Hojo, M., Hollister, S.J., 2006. Framework for optimal design of porous scaffold microstructure by computational simulation of bone regeneration. Biomaterials 27, 3964–3972.
Bathe, K.J., 1996. Finite Element Procedures. Prentice-Hall, New Jersey.
Bil, M., Ryszkowska, J., Roether, J.A., Bretcanu, O., Boccaccini, A.R., 2007. Bioactivity of polyurethane-based scaffolds coated with Bioglass. Biomed. Mater. 2, 93–101.

Boccaccini, A.R., Chen, Q., Lefebvre, L., Gremillard, L., Chevalier, J., 2007. Sintering, crystallisation and biodegradation behaviour of Bioglass®-derived-glassceramics. Faraday Discuss 136, 27–44.
Chen, Q.Z., Thompson, I.D., Boccaccini, A.R., 2006a. 45S5 Bioglass-derived glassceramic scaffolds for bone tissue engineering. Biomaterials 27, 2414–2425.
Chen, Q.Z., Boccaccini, A.R., 2006b. Poly(D,L-lactic acid) coated 45S5 Bioglass-based scaffolds: processing and characterization. J. Biomed. Mater. Res. A 77, 445–457.
Clark, A.R., Pantano, C.G., Hench, L.L., 1976. Auger spectroscopic analysis of Bioglass corrosion films. J. Am. Ceram. Soc. 59, 37–39.
Diego, R.B., Más-Estellés, J., Sanz, J.A., García-Aznar, J.M., Salmerón-Sánchez, M., 2007. Polymer scaffolds with interconnected spherical pores and controlled architecture for tissue engineering. Fabrication, mechanical properties and finite element modeling. J. Biomed. Mater. Res. B 81, 448–455.
Fu, Q., Rahaman, M.N., Bal, B.S., Huang, W., Day, D.E., 2007. Preparation and bioactive characteristics of a porous 13-93 glass, and fabrication into the articulating surface of a proximal tibia. J. Biomed. Mater. Res. A 82, 222–229.
Gopferich, A., 1997. Polymer bulk erosion. Macromolecules 30, 2598–2604.
Guarino, V., Causa, F., Ambrosio, L., 2007. Bioactive scaffolds for bone and ligament tissue. Expert Rev. Med. Devic. 4, 405–418.
Guldberg, R.E., Hollister, S.J., Charras, G.T., 1998. The accuracy of digital image-based finite element models. J. Biomech. Eng. 27, 433–444.
Han, X., Pan, J., 2009. A model for simultaneous crystallisation and biodegradation of biodegradable polymers. Biomaterials 30, 423–430.
Hench, L.L., Splinter, R.J., Allen, W.C., Greenlee, T.K., 1971. Bonding mechanisms at the interface of ceramic prosthetic materials. J. Biomed. Mater. Res. 2, 117–141.
Hench, L.L., Paschall, H.A., 1973. Direct chemical bond of bioactive glass–ceramic materials to bone and muscle. J. Biomed. Mater. Res. Symp. 4, 25–42.
Hench, L.L., Stanley, H.R., Clark, A.E., Hall, M., Wilson, J., 1991. Dental application of Bioglass implant. In: Bonfield, E., Hastings, G.W., Tanner, K.E. (Eds.), Bioceramics, vol. 4. Butterworth Heinemann, Oxford, UK, pp. 232–238.
Hench, L.L., West, J.K., 1996. Biological applications of bioactive glasses. Life. Chem. Rep. 13, 187–241.
Hench, L.L., 1998. Biomaterials: a forecast for the future. Biomaterials 19, 1419–1423.
Hench, L.L., Polak, J.M., 2002. Third-generation biomedical materials. Science 295, 1014–1017.
Hibbit, Karlsson, Sorensen, 2001. Abaqus Users Manual v.6.2. HKS Inc., Pawtucket, RI.
Hughes, T.J.R., 2000. The Finite Element Method: Linear Static and Dynamic Finite Element Analysis, second ed. McGraw-Hill, Dover, New York.
Hutmacher, D.W., 2000. Scaffolds in tissue engineering bone and cartilage. Biomaterials 21, 2529–2543.
Jerome, R., Maquet, V., 1997. Design of macroporous biodegradable polymer scaffolds for cell transplantation. Mater. Sci. Forum 250, 15–42.
Knabner, P., van Duijn, C.J., Hengst, S., 1995. An analysis of crystal dissolution fronts in flows though porous media. Part 1: compatible boundary conditions. Adv. Water Resour. 18, 171–185.
Kokubo, T., Kushitani, H., Sakka, S., Kitsugi, T., Yamamuro, T., 1990. Solutions able to reproduce in vivo surface-structure changes in bioactive glass–ceramic A-W. J. Mater. Res. 24, 721–734.
Li, P., Yang, Q., Zhang, F., Kokubo, T., 1992. The effect of residual glassy phase in a bioactive glass–ceramic on the formation of its surface apatite layer in vitro. J. Mater. Sci. Mater. Med. 3, 452–456.
Lin, C.Y., Kikuchi, N., Hollister, S.J., 2004. A novel method for biomaterial scaffold internal architecture design to match bone elastic properties with desired porosity. J. Biomech. 37, 623–636.
Livingston, T., Ducheyne, P., Garino, J., 2002. In vivo evaluation of a bioactive scaffold for bone tissue engineering. J. Biomed. Mater. Res. 62, 1–13.
Reddy, J.N., 1993. An Introductory Course to the Finite Element Method, second ed. McGraw-Hill, Boston.
Rezwan, K., Chen, Q.Z., Blaker, J.J., Boccaccini, A.R., 2006. Biodegradable and bioactive porous polymer/inorganic composite scaffolds for bone tissue engineering. Biomaterials 27, 3413–3431.
Roether, J.A., Boccaccini, A.R., Hench, L.L., Maquet, V., Gautier, S., Jerome, R., 2002a. Development and in vitro characterisation of novel bioresorbable and bioactive composite materials based on polylactide foams and Bioglasss for tissue engineering applications. Biomaterials 23, 3871–3878.
Roether, J.A., Gough, J.E., Boccaccini, A.R., Hench, L.L., Maquet, V., Jerome, R., 2002b. Novel bioresorbable and bioactive composites based on bioactive glass and polylactide foams for bone tissue engineering. J. Mater. Sci: Mater. Med. 13, 1207–1214.
Sanz-Herrera, J.A., 2008a. Multiscale simulation of bone regeneration in tissue engineering processes. Ph.D. Thesis, University of Zaragoza, Spain.
Sanz-Herrera, J.A., García-Aznar, J.M., Doblaré, M., 2008b. A mathematical model for bone tissue regeneration inside a specific type of scaffold. Biomech. Model. Mech. 7, 355–366.
Sanz-Herrera, J.A., García-Aznar, J.M., Doblaré, M., 2008c. Micro-macro numerical modelling of bone regeneration in tissue engineering. Comput. Methods Appl. Mech. Eng. 197, 3092–3107.
Sanz-Herrera, J.A., Kasper, C., van Griensven, M., García-Aznar, J.M., Ochoa, I., Doblaré, M., 2008d. Mechanical and flow characterization of Sponceram carriers: evaluation by homogenization theory and experimental validation. Biomed. Mater. Res. B: Appl. Biomater. 87, 42–48.
Sanz-Herrera, J.A., García-Aznar, J.M., Doblaré, M., 2009a. On scaffold designing for bone regeneration: a computational multiscale approach. Acta Biomater. 5, 219–229.

Sanz-Herrera, J.A., García-Aznar, J.M., Doblaré, M., 2009b. A mathematical approach to bone tissue engineering. Proc. Roy. Soc. A 367, 2055–2078.

Tilocca, A., 2009. Structural models of bioactive glasses from molecular dynamics simulations. Proc. Roy. Soc. A 465, 1003–10027.

van Noorden, T.L., Pop, I.S., 2008. A Stefan problem modelling crystal dissolution and precipitation. IMA J. Appl. Math. 73, 393–411.

Vitale-Brovarone, C., Verne, E., Robiglio, L., Appendino, P., Bassi, F., Martinasso, G., Muzio, G., Canuto, R., 2007. Development of glass–ceramic scaffolds for bone tissue engineering: characterisation, proliferation of human osteoblasts and nodule formation. Acta Biomater. 3, 199–208.

Wake, M.C., Patrick, C.W., Mikos, A.G., 1994. Pore morphology effects on the fibrovascular tissue growth in porous polymer substrates. Cell Transplant. 3, 339–343.

Wang, Y., Pan, J., Han, X., Sinka, C., Ding, L., 2009. A phenomenological model for the degradation of biodegradable polymers. Biomaterials 29, 3393–3401.

Wilson, J., Low, S.B., 1992. Bioactive ceramics for periodontal treatment: comparative studies in the Patus monkey. J. Appl. Biomater. 3, 123–169.

Wilson, J., Yli-Urpo, A., Risto-Pekka, H., 1993. Bioactive glasses: clinical applications. In: Hench, L.L., Wilson, J. (Eds.), An Introduction to Bioceramics. World Scientific, Republic of Singapore, pp. 63–74.

Yamamuro, T., 1990. Reconstruction of the iliac crest with bioactive glass–ceramic prostheses. In: Yamamuro, T., Hench, L.L., Wilson, J. (Eds.), Handbook of Bioactive Ceramics: 1. Bioactive Glasses and Glass–Ceramics. CRC Press, Boca Raton, FL, pp. 335–342.

Yunos, D.M., Bretcanu, O., Boccaccini, A.R., 2008. Polymer–bioceramic composites for tissue engineering scaffolds. J. Mater. Sci. 43, 4433–4442.

Zienkiewicz, O.C., Taylor, R.L., 2000. The Finite Element Method, fifth ed. Butterworth-Heinemann, Oxford.